New Design Ideas
Vol.8 | Special Issue | ICCAUA2024, pp.1-23
https://doi.org/10.62476/ndisi.01

DESIGN ADVANCES IN URBAN IMPERVIOUS SURFACE EXTRACTION: LEVERAGING K-DISTRIBUTIONS, GLCM, RAYLEIGH AND NAKAGAMI WITH VHR SAR TECHNOLOGY

Salvatore Polverino[1*], Hourakhsh Ahmad Nia[2], Rokhsaneh Rahbarianyazd[2]

[1]Department Training and Internationalization, Ordine Architetti Pianificatori Paesaggisti Conservatori di Napoli e Provincia, Napoli, Italy
[2]Department of Architecture, Faculty of Engineering and Natural Sciences, Alanya University, Alanya, Türkiye

Abstract. The design innovations in the extraction of urban impervious surfaces have played a vital role in using Very High-Resolution Synthetic Aperture Radar technology. Advanced radar technologies are integrated here, with the inclusion of various statistical methodologies like Rayleigh, Nakagami and K-distributions in integration with the Gray Level Co-occurrence Matrix, Principal Component Analysis and Gabor filters. For analyzing the intensity data of SAR imagery in regard to environmental monitoring, as well as Electronic Warfare has been used in the research. The Shapiro-Wilk test shows the beginning of this work; investigating the departure from normality, the material properties and environmental factors were viewed to have a significant effect on the variation in pixel intensities. Further, the analysis of data with heterogeneity based on some measures of Skewness and Kurtosis was performed. This research is based on design-centred approaches for reducing state noise and enhancing target tracking in complex scenarios by performing textural analysis using techniques such as GLCM, PCA and Kalman filtering. Integration optimizes VHR SAR for enhanced situational awareness and effective detection in an urban landscape. This therefore places a great magnitude on the influence of design on the modification of material properties and effective radar detection.

Keywords: *Design optimization for urban detection, Electronic Warfare (EW), Very High-Resolution Synthetic Aperture Radar (VHR SAR), Rayleigh distribution, Gray Level Co-occurrence Matrix (GLCM), Kalman filtering, Situational Awareness (SA).*

***Corresponding Author:** Salvatore Polverino, Ordine Architetti Pianificatori Paesaggisti Conservatori di Napoli e Provincia, Napoli, Italy, Tel.: 081/4238259, e-mail: formazione@napoli.archiworld.it, polverinosalvatore@outlook.com*

Received: *15 June 2024;* ***Accepted:*** *18 August 2024;* ***Published:*** *10 October 2024.*

1. Introduction

In contemporary Electronic Warfare (EW), achieving and maintaining operational superiority is critically dependent on the performance of advanced technological systems.

Very High-Resolution Synthetic Aperture Radar (VHR SAR) imaging stands out as a crucial tool, offering precise imagery that enhances the ability to monitor, detect and analyze various targets and environments, trusted for forensic evaluation versatile for unauthorized built land cover, hybrid-oriented, as for SAR-VHF Unmanned Aerial

How to cite (APA):
Polverino, S., Nia, H.A. & Rahbarianyazd, R. (2024). Design advances in urban impervious surface extraction: Leveraging K-distributions, GLCM, Rayleigh and Nakagami with VHR SAR technology. *New Design Ideas, 8*(Special Issue), 1-23 https://doi.org/10.62476/ndisi.01

Vehicle frameworks (Goriachkin *et al*., 2022) and grounded across built environment landmarks (Abdulla & Abdelmonem, 2023; Madrigal, 2018); damage detection has been also proven in terms of both anthropic (Dong *et al*., 2013) and natural (Gokon *et al*., 2017) anomalies; by acknowledging Multi-Criteria Decision Analysis (MCDA) (Janalipour *et al*., 2017) and cartographic overlays (Bouziani *et al*., 2010), retrieved from geodatabases, we aim to diversify method land change techniques, whose planning is also agreed by authors Reba and Seto (2020).

By deeply understanding these interactions, this applied research aims to advance the methodologies used in Electronic Warfare (EW), optimizing radar performance (Ruiz *et al*., 2020; Zhang *et al*., 2022) in urban (Softaoğlu, 2019) and natural environments (Yang *et al*., 2019), proposing a promoted Multistage process for SAR Image Segmentation and refinement (Ning *et al*., 2024).

In accordance with the process, we begin with Segmentation Initialization, where input SAR images undergo initial breakdown using edge detection techniques to identify significant features. With this in mind, as illustrated in Figure 1, the results are rendered in coarse segmentation outputs, which are then refined through an iterative refinement process involving iterative adjustments, such as applying GLCM (Christaki *et al*., 2022) and Gabor filters to enhance texture analysis. The refined results are compared with ground truth data using an Error Metric, guiding further adjustments. The lower path incorporates a Kalman filter-based refinement process (Subrahmanyam *et al*., 2008), to further refine predictions and minimize errors. Corroborated by these results, the final output is a segmented image that closely matches the ground truth, suitable for detailed analysis and impact prediction.

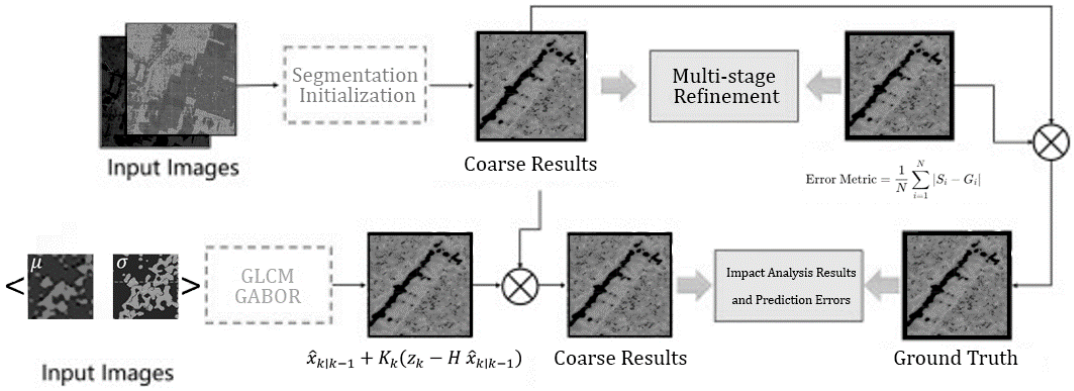

Figure 1. Hierarchical refinement: Multi-stage Feature Extraction for Ground Truth prediction

2. Background and Context

This study makes significant strides in enhancing Very High-Resolution Synthetic Aperture Radar (VHR SAR) for Electronic Warfare (EW) and environmental monitoring, with a clear focus on improving Situational Awareness (SA) in heterogeneous sites.

To encapsulate the integration of advanced filtering techniques, all of them non-destructive, we recognize a strong step toward refining radar image quality and target detection, directly contributing to heightened SA. While the background may appear broad, it effectively underscores the critical importance of operating in the context of sensitive environments, delving into the scientific lecture of surfaces of built structures,

enabling these advancements to improve both spatial resolution and image processing techniques (Esch *et al*., 2010), making SAR systems more reliable in detecting subtle changes in target characteristics (Chen *et al*., 2024).

2.1. Problem Statement and Research Gap

The challenge of enhancing radar performance in complex and dynamic environments, such as conflict zones, is critical, particularly when traditional methods fall short in rapidly changing and hostile settings (Odunlade & Abegunde, 2023). Critically, this applied research seeks to address this gap by optimizing detection and monitoring through advanced radar signal processing and analysis of the built environment as a track record of our departmental Mission at Ordine Architetti Napoli for heritage protection.

Given the constraints imposed by the primary problem, we face the specialistic understanding of how built entities and technological advancement influence the performance of VHR SAR imaging: this gap of understanding, among Architects subscribers, limits the effectiveness of radar-based strategies, particularly in complex and off-limits environments.

In light of this research gap in the application of SAR performance, we take into consideration that these techniques are well-established in EW, albeit their potential to optimize SAR imaging in challenging environments remains underestimated or partially maintained over new integrations.

Acknowledging the experimental conditions, we integrate advanced textural methods, such as Gray Level Co-occurrence Matrix (GLCM) analysis (Soh *et al*., 1999) and Principal Component Analysis (PCA), in the pre-processing of VHR SAR imaging; recognizing the relevance of these methods in the scientific community, we then provide critical insights into various alternatives in terms of radar image contrast, which are essential for accurate material characterization and anomaly detection.

By the same token, factoring in the analytical techniques used, we also investigate a gap in the use of modern algorithmic tools, as recently highlighted by researchers Peng et al. (2023), featuring a combination of Gabor (1946) and Kalman filters (Luo *et al*., 2023), to improve the interpretation and accuracy of SAR imagery.

Upon consideration, this quantitative investigation addresses the critical need for advanced radar technologies by bridging research gaps in material impact analysis, scattering parameterization, feature extraction, and computational enhancements.

2.2. Limitations and analytical perspectives on the first VHR SAR dataset

The Shapiro-Wilk test results revealed that all extracted features (Makmur *et al*., 2023) for this initial test in a similar analytical industrial context, a contour-based setting (Ersahin *et al*., 2010), exhibiting significant deviations from normality, as evidenced by the extremely low *p*-values for each feature. This approach is essential for determining the tolerance intervals used to assess the accuracy of SAR-based measurements, particularly in agricultural applications where precise area measurements are critical (Pluto-Kossakowska & Kerdiles, 2007).

In agreement with a grid of approximately 3000 points with a vertical spacing of 11.68 pixels and a horizontal spacing of 13.25 pixels, we obtained for mean intensity, the Shapiro-Wilk statistic of 0.907 suggested a limited moderate central tendency, but the *p*-value of 1.242×10^{38}, confirming a substantial departure from a normal distribution; this deviation could be due to uneven lighting, shadows or highlights within the image,

causing a skewed distribution (Kuruoglu & Zerubia, 2004) of pixel intensities, i.e. despite the moderate Shapiro-Wilk statistic, the significant *p*-value indicated that the distribution of statistical factors (Martín-de-Nicolás *et al*., 2014), such as mean intensity values and standard deviation, are not normal also confirmed by values $\mu \approx 166.55$ and $\sigma \approx 23.12$.

Secondly, the standard deviation of pixel intensities shows a Shapiro-Wilk statistic of 0.967 and a *p*-value of 3.227×10^{-25}: although the high statistic suggests that the distribution of standard deviation values was closer to normality compared to the mean intensity, the low *p*-value still indicates a strong deviation from normality; this suggests that whilst the variability in pixel intensities is somewhat consistent, there are outliers or non-uniform variations within the image, i.e. $\mu \approx 19.46$ and $\sigma \approx 9.69$, possibly due to regions with significant texture or contrast changes.

Thirdly, skewness, which measures the asymmetry of the distribution, had a Shapiro-Wilk statistic of 0.965 and a *p*-value of 2.075 × 10 -18: the high statistic suggests a degree of symmetry, but the extremely low *p*-value indicating a significant departure from normality, i.e. this asymmetry was likely caused by areas with drastically. The results for the initial pixel intensity distributions are illustrated in Figure 2 where: (a) the histogram reveals the distribution of mean intensity values across the dataset and the box plot adjacent to the histogram indicates a moderate spread in the intensity values, with an interquartile range (IQR) of 13.83, showing that the middle 50% of the data falls within this range. The skewness of -0.187 suggests a slight left skew, indicating that the data has a longer tail on the lower end of the intensity spectrum; (b) the IQR of 11.51 shows that there is significant clustering of standard deviation values within this range, reflecting a consistent degree of variation across the dataset; (c) the IQR of 13.74, indicates variability in the asymmetry of the data across different regions; (d) the variability in the peaked-ness of the data appears to be critical for identifying areas of high-intensity concentration or dispersion within the radar images.

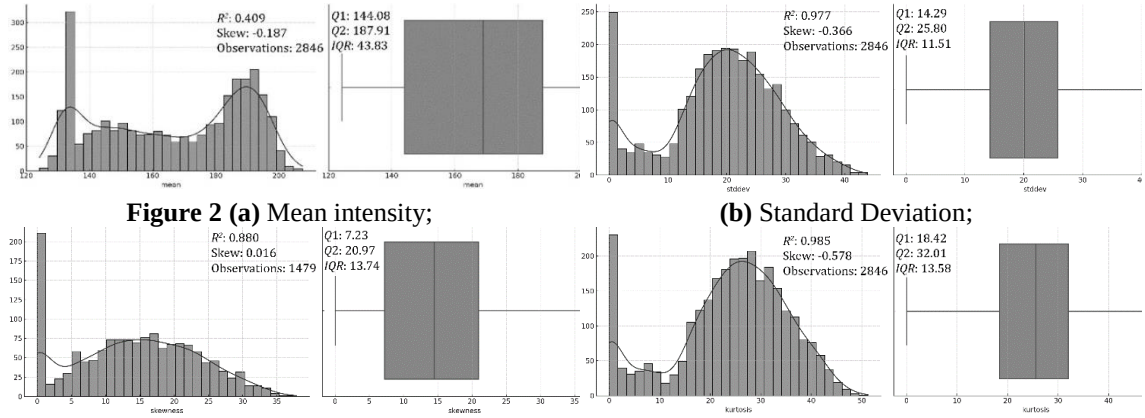

Figure 2 (a) Mean intensity; **(b)** Standard Deviation; **(c)** Skewness; **(d)** Kurtosis.

To this extent, Figure 3 showcases their corresponding (left) original image; (centre) edge detection using gradient operators; and (right) watershed segmentation into distinct regions, introducing an object-based approach (Hussain *et al*., 2013).

Figure 3. Multistage Image Processing for SAR Data Analysis

Alternatively, Figure 4 emphasizes the selected Gabor representation of planar symmetry for accurate detection of structural features.

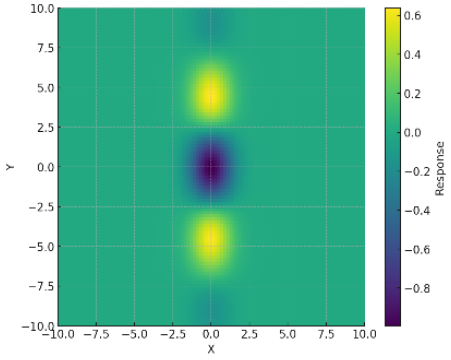

Figure 4. Planar Symmetry Analysis

Illustrated through evidence, Figure 5 provides valuable insights in terms of 3D Gabor filter responses ($\gamma = 5.1$, $\sigma = 2$, $\psi = 3.1$), characterized by a central peak and periodic oscillations.

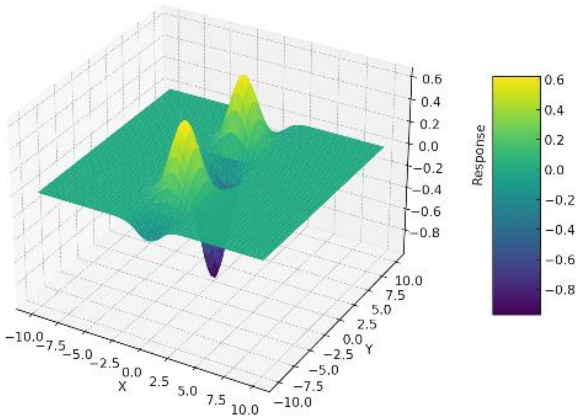

Figure 5. Characterization of Gabor filter responses, highlighting central peaks and periodic oscillations

2.3. Pixel value distribution and iterative variance VHR μ-σ Image data

A critical finding in this research is the impact of variable lighting and texture, further confirmed by double-bounce areas (Ferro *et al.*, 2013), on pixel value distribution within images, resulting in significant non-normality. This deviation from normality is

quantified by a mean (μ) of approximately 14.14 and a standard deviation (σ) of approximately 9.17.

This non-normal distribution is further evidenced by the kurtosis, which measures the peakedness of the distribution. The Shapiro-Wilk test produced a statistic of 0.951 and a *p*-value of 7.365×10^{-30} indicating a significant deviation from normality. High kurtosis values suggest the presence of outliers or extreme values, likely resulting from sharp edges, noise or distinct features within the image, leading to pronounced peaks in the intensity distribution. The mean (μ) was approximately 24.23 and the standard deviation (σ) was approximately 11.45.

In the context of iterative analysis for the X-band (Dabiri *et al*., 2015), the variation curve of variance and contrast with iteration shows that the horizontal Gabor metric values for local variance and contrast fluctuate over time. The central blue box in the visual representation delineates the non-layered region, which was used to compute the average variance. As displayed in Figure 6, the Dense Grid Overlay highlights the related pointedness, serving as an initial parameter of stability and changes in image properties during processing.

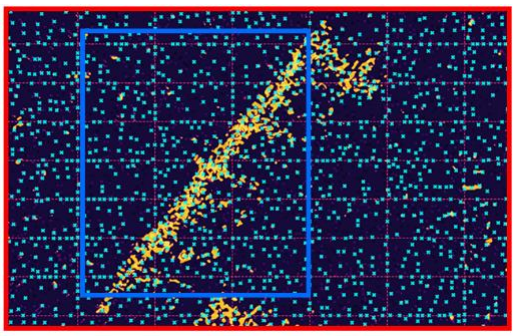

Figure 6. Non-layered and layered regions of detected peaks for iterative variance analysis

By the same token, Figure 7, supports the obtained Radargram obtained through horizontal Gabor enhancement, which superimposes the correlation on the hypothesis of interpolated radar echo data.

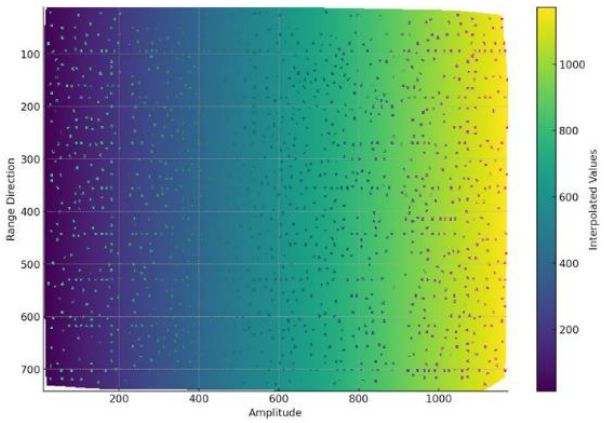

Figure 7. Correlation analysis of Gabor filter parameters with VHR SAR data for improved image feature extraction

Consistent with the correlation, we observe that the logarithmic and linear representations of local variance in the non-layered region provide complementary views.

While the logarithmic scale in Figure 8 (a) is useful for monitoring small changes, suggesting a steady and gradual decrease across iterations, emphasizing convergence towards homogeneity in the region. This indicates that as iterations progress, the changes in variance become less significant, pointing to a stabilization of texture features. In contrast, the linear scale in Figure 8 (b) offers a clearer interpretation of how variance is reduced significantly early on. Together, these perspectives can help optimize the iterative process by balancing early-stage rapid changes with late-stage fine-tuning.

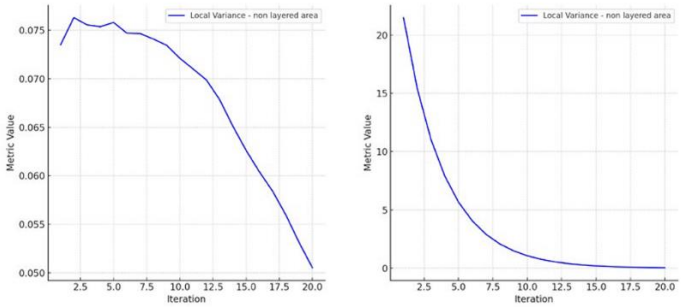

Figure 8 (a) Logaritmic local variance of non-layered region; **(b)** Local variance of non-layered region

Regarding the layered region, Figure 9 (a) illustrates the observated trend of a gradual and steady decrease in contrast across iterations, highlighting the ongoing process of smoothing and the progressive reduction of intensity differences between adjacent pixels, leading to a more homogeneous appearance. In contrast, Figure 9 (b) emphasizes the significant initial reduction in contrast, suggesting that the majority of the smoothing effect occurs early in the process.

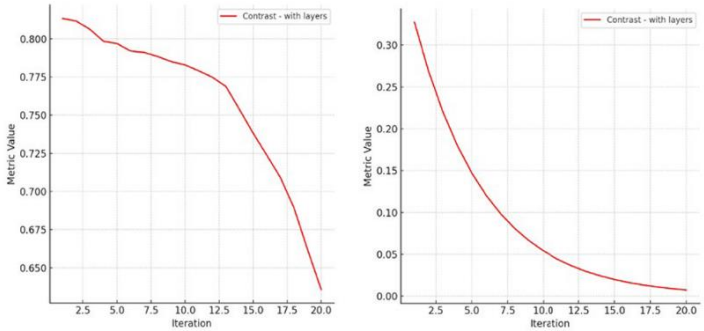

Figure 9 (a) Logarithmic contrast of with-layers layered regions;
(b) Contrast of with-layer layered regions.

2.4. Parameterization of Gabor Filters Across Diverse Operational Scenarios

Parallel to the Gabor enhancement, we priorly examined its correlation and a defined set of parameters, under various operational conditions. The focus was on several critical parameters, such as gamma (γ), sigma (σ), psi (ψ), theta (θ) and lambda (λ), which influence the behaviour of Gabor filters in analyzing radar imagery. These parameters, along with the Rayleigh (Gomes *et al*., 2019) sigma (σ), mu-sigma ($N\mu$), omega ($N\omega$), shape parameter ($\nu\kappa$) and the second moment ($\mu\zeta 2$), provide insights into the statistical

properties of detected peaks in the radar data. Table 1 reports how each row corresponds to a specific radar optical scenario, ranging from *Critical* and *High Risk* to more routine conditions like *Recon* and *Observation*.

Table 1. Parameterization of Gabor filters and *Recon* values corresponding to detected peaks

Radargram	γ	σ	ψ	θ	λ	**Rayleigh** σ	N_μ	N_ω	v_K	μ_{ξ^2}
Critical	1.00	5.00	0.90	1.20	16.00	180.35	0.040	0.035	64.53	-
High Risk	0.80	5.00	1.00	0.80	18.00	180.31	0.040	-	70.58	-
Moderate	0.80	2.50	1.10	1.50	14.00	180.29	0.040	0.00036	70.03	-
Low Risk	1.00	4.00	0.50	1.50	20.00	180.31	0.040	-	70.58	-
Surveillance	0.70	4.00	1.30	0.90	12.00	171.00	0.041	4.98	58.97	-
Monitoring	1.50	6.00	0.90	1.10	12.00	124.07	0.043	17.23	47.74	-
Observation	1.10	5.00	1.50	1.30	10.00	75.70	0.040	-	-	-
Patrol	0.60	4.00	2.00	1.20	10.00	37.53	0.061	75.97	1.00	1.00
Recon	**0.50**	**3.00**	**0.78**	**1.57**	**10.00**	**37.53**	**0.081**	**24.50**	**0.30**	**0.21**
Watch	1.30	4.00	2.00	0.70	12.00	17.92	0.081	24.50	0.30	0.21
Guard	1.30	4.00	2.00	0.70	12.00	15.19	-	-	-	-
Check	0.90	4.00	1.80	1.40	14.00	7.40	-	-	-	-
Scan	1.10	2.00	1.50	1.40	8.00	68.78	0.050	37.17	0.78	0.58
Track	0.70	3.00	2.20	0.90	20.00	0.00	-	-	-	-
Sweep	1.20	3.00	1.80	1.00	20.00	27.20	0.067	25.54	0.38	0.26

2.5. Effect of Gabor Filters on Consistency and Spatial Distribution in Radargram

The radargram of detected peaks shows a correlation value of -0.10, indicating a weak negative correlation between the original features and those after the application of the Gabor filter. In like manner, this weak negative correlation implies that the spatial distribution of the features in the filtered image does not closely follow the original distribution: for the original features, scrutinized in Figure 10 (a), the mean was 109.00 with a standard deviation of 79.06, which suggests a wide spread of values around the mean, reflecting considerable variability.

To substantiate this statistical trend, the filtered features exhibit a significantly higher mean of 250.29 and a much lower standard deviation of 20.96. Correspondingly, this substantial increase in mean value, coupled with the reduction in variability, suggests that the Gabor filter enhances specific aspects of the features, pertaining to a more uniform distribution post-filtering. Additionally, a further comparison with its post-processed version, compared in Figure 10 (b), attests that the original features had a mean of 128.49 with a standard deviation of 76.25, again indicating a broad spread around the mean, similar to the first dataset. Reflectively, the filtered features showed a mean of 222.47 and a standard deviation of 25.99, reinforcing the conclusion that the filtering process not only enhances feature consistency but also raises the mean values.

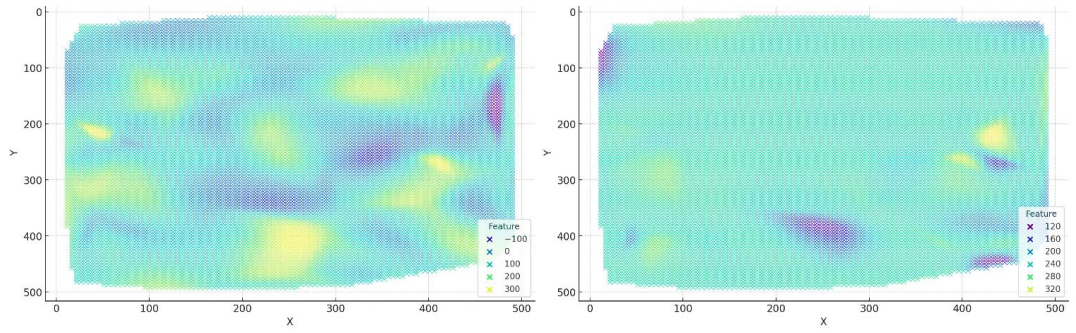

Figure 10 (a;b). Radargram of Detected Peaks: feature distributions before and after Gabor filtering

2.6. Gabor Filters on Consistency and Spatial Distribution in Radargram

Integrating the insights from the Radargram Gabor analysis with the evaluation of Rayleigh distribution (Greenspan, 1971) and Nakagami models, it becomes evident that the underlying principles of improving feature clarity and consistency are shared across both domains.

Just as the Gabor filter enhances the statistical properties of radar images by increasing mean values and reducing variability, the Akaike Information Criterion (AIC) and Mean Squared Error (MSE) metrics (Zhou *et al*., 2009) support the hypothesis of the best trade-off between Goodness-of-Fit (GoF) supported by (Sagrillo *et al*., 2022) and outperforming regions with asymmetry, positive skewness and heavy tails and simplicity.

Conveniently, the AIC-MSE model avoids overfitting by accounting k independently adjusted parameters, (Akaike, 1974) and using Mean Squared Error (MSE), (Zhou & Bovik, 2009). Additionally, (Chang *et al*., 2016) provided crucial insights into model accuracy and selection, often yielding consistent results across various datasets.

The AIC-MSE model serves as a tool to assess and refine the predictive accuracy and efficiency of wireless communication models. By applying these metrics, much like the Gabor filter was used to stabilize and clarify image features, this framework enhances understanding by selecting the optimal model in complex environments, such as urban multipath channels (Shahzad *et al*., 2019).

This integration is also applied in Rayleigh and Nakagami models (Liebenberg & James, 2023), which indicate identical MSE values of 0.455. MSE measures the average squared differences between observed and predicted values, indicating the predictive accuracy of the models. The identical MSE values imply equivalent predictive performance between the two models.

The AIC values for both models were approximately -11.736, measuring the trade-off between model fit and complexity by penalizing excessive parameters. Lower AIC values indicate better model efficiency, balancing fit and simplicity. The identical AIC values suggest that both models achieve similar efficiency in capturing data patterns while avoiding overfitting.

These consistent MSE and AIC values support the conclusion that the Rayleigh and Nakagami fading channels, for the observed random variables (Salo *et al*., 2006), as also dually proposed by researchers Fotohabady and Fatin (2011), can be compared in terms of efficiency, qualifying convenience of the second, by consuming less power than Rayleigh channels: Nakagami behaves in a more efficient manner for wireless communication scenarios applied in urban multipath environments.

Supporting this duality, we observe that both models (Tegos *et al*., 2022), perform similarly in terms of received Signal-to-Noise Ratio (SNR), falling below a certain threshold γ_{thr}, according to the CDF distribution, and thus accomplish equally for this dataset. However, further validation with additional datasets or cross-validation techniques is recommended to confirm the robustness and generalizability of these models. Figure 11 illustrates a Box plot showing the N_ω, v_K and μ_{ξ^2} Values related to the statistical distribution of key Gabor filter parameters across different risk levels. In line with this consistency, the comparison of both MSE and AIC is referenced in Figure 12 for VHR SAR data analysis, with Rayleigh models yielding values of 9.29×10^9 and 116.76, and Nakagami models yielding 5.97×10^9 and 116.55, respectively.

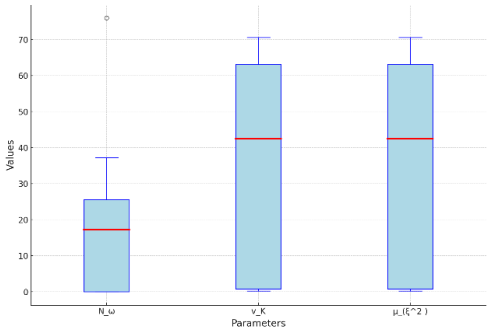

Figure 11. Box Plot of Gabor Filter Parameters

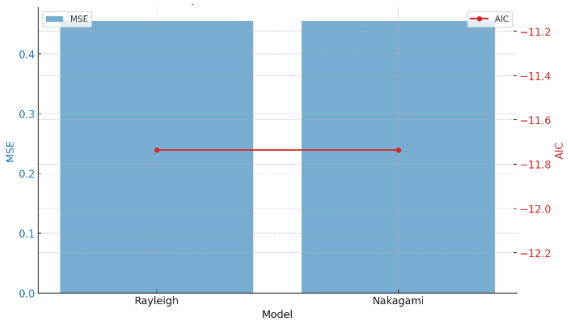

Figure 12. Comparison of MSE and AIC for Rayleigh.

These findings suggest that the image contains complex characteristics related to shadow analysis, which are crucial for the RCS value of the first building, albeit limited to the asphalt-built surroundings. Factors such as varying lighting, texture and distinct features contribute to the non-normal distributions of these features.

Consequently, the focus shifted to a small building used for Industrial R&D, with a white metal roof, as visualized in Figure 13 (a) pertaining to Mean Intensity. The calculations required the implementation of a Gabor filter to better capture the shadow patterns relative to the non-metallic main body of the industrial complex's surface, referenced in Figure 13 (b) for Standard Deviation.

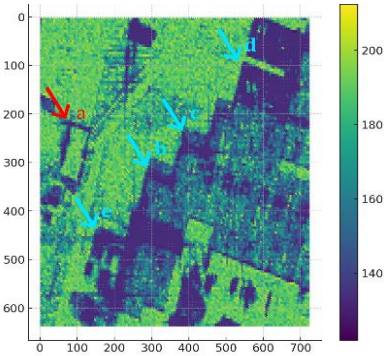

Figure 13. (a) Mean Intensity

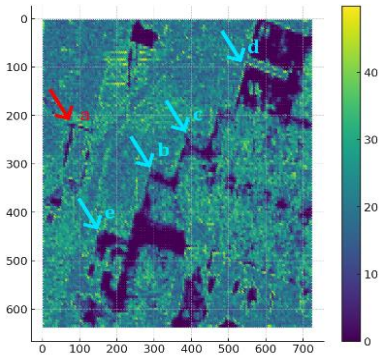

(b) Standard Deviation

Additionally, an overhanging building was ambiguously camouflaged by the shadow (c), or only partially (d), and was therefore discarded from the selection.

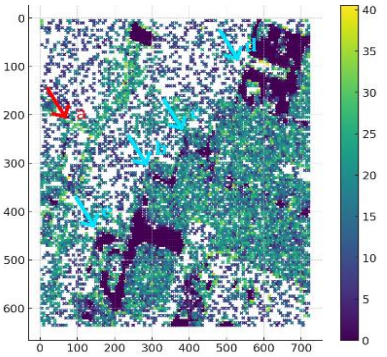

Figure 13. (c) Skewness

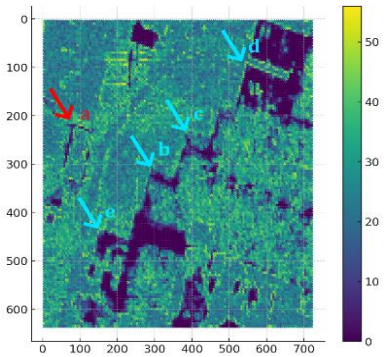

(d) Kurtosis

2.7. HH Multistage: Morphology detection and GLCM with Kalman covariance

The analysis of HH polarization for VHR SAR datasets shows significant deviations in key metrics for metallic-roof buildings. Rayleigh and Nakagami distributions were tested, but the Rayleigh model, with a sigma of 7.37, underestimated the intensity peaks of the data. Nakagami and K-distributions performed better, particularly in complex terrains. Across multiple scenarios, including GLCM Entropy (Puetz *et al*., 2006) and PCA (Singh *et al*., 2011), empirical data peaked at 10-15 intensity units, but the Rayleigh model consistently misaligned with the observed peaks. Although Nakagami and K-distributions executed well, they still displayed discrepancies. A detailed 3D visualization in Figure 14 highlights these findings, with red indicating areas of higher anomaly impacts.

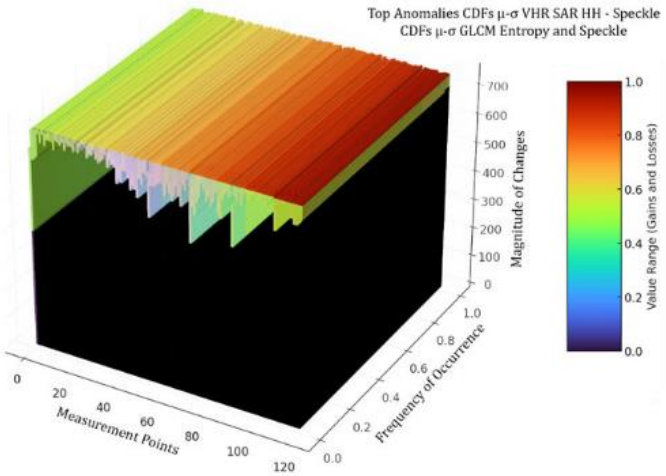

Figure 14. CDFs of VHR SAR HH Data

2.8. Impact of Variability on Feature and Anomaly Detection in SAR Imaging

The series of figures presented, with the respective comparisons in Figures 15, 16, 17 and 18, provide a comprehensive analysis of various aspects related to VHR SAR imaging, particularly focusing on feature impacts, Entropy and Dissimilarity.

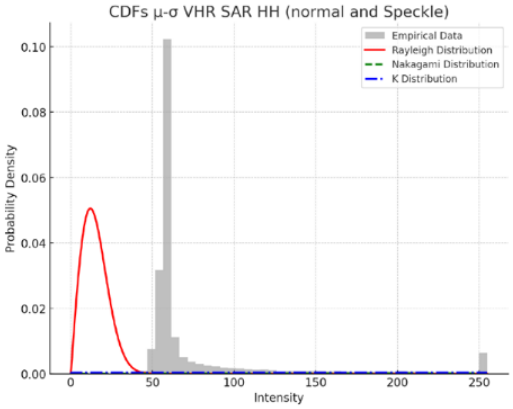

Figure 15. GLCM Entropy and Dissimilarity

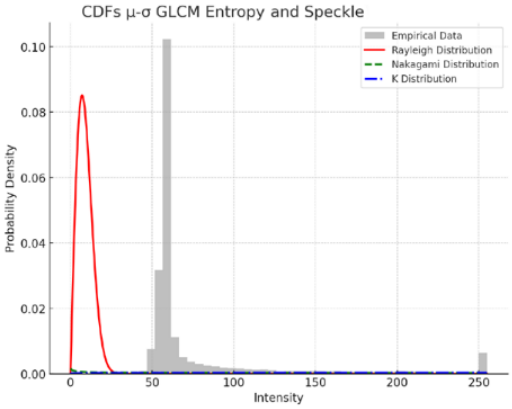

Figure 16. Multistage of feature impacts on prediction errors

The most evident anomaly that emerged is the Optical ground truth cluster, represented in grey colour, which is related to μ-σ GLCM PCA and GLCM Entropy.

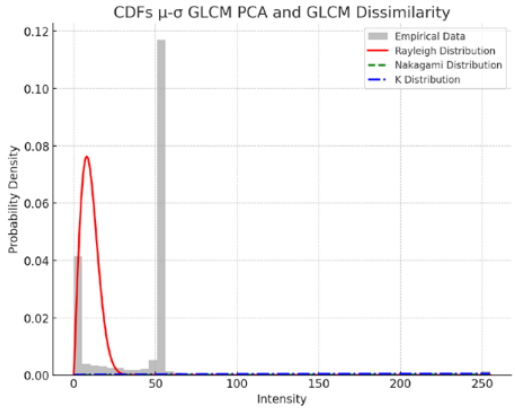

Figure 17. Feature Impact Analysis

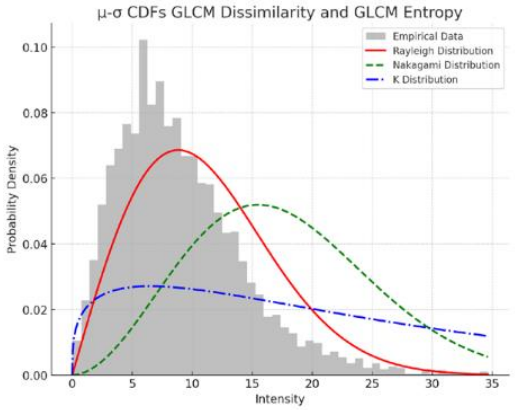

Figure 18. Significant gains and minimal losses

In support of the statistical behaviours, the estimated scale parameters for the images are respectively: $\sigma_1 = 9.73$, $\sigma_2 = 5.68$, $\sigma_3 = 6.38$, $\sigma_4 = 6.98$. The overall comparison is confirmed in Figure 19.

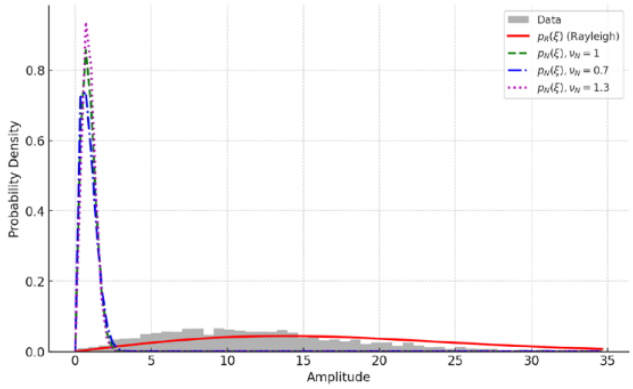

Figure 19. Anomaly Impact Analysis

2.9. Maximum Likelihood Estimation for K-Distribution and Nakagami

Building on the earlier discussion of statistical models for radar data analysis, the Nakagami distribution is now examined for its flexibility and superior fit when compared to the Rayleigh model, particularly in handling complex data patterns. The Nakagami dispersal, while offering greater flexibility (Mesleh *et al*., 2022) with two parameters (v and Ω), provides a recovering and better fit than the Rayleigh model: the shape parameter. v_N For Nakagami was computed as formulated in Equation 1. Specifically, the computed shape parameter value $\tilde{v}_N = 0.9355$ indicates that the Nakagami model is less likely to produce erroneous results. The parameters are defined as: $v = \ln\left(\frac{\tilde{\mu}\,\xi^2}{F}\right)$ and $F = \left(\prod_{q=1}^{n\ smp} \xi_q^2\right)^{\frac{1}{n\ smp}}$.

$$\text{follows: } v_N = \begin{cases} \dfrac{0.5000876 + 0.1648852\ \mathrm{v} + 0.0544274\ v^2}{v} \\ \dfrac{8.98919 + 9.059950\ v + 0.9775373\ v^2}{v\ (17.79728 + 11.968477)\ v + v^2} \end{cases}; \quad \begin{matrix} \text{if } 0 < v \leq 0.5772 \\ \text{if } 0.5772 < v\ < 0.5772 \end{matrix} \quad (\ldots)$$

Equation 1. Shape Parameter Calculation for the Nakagami Distribution

Due to the heterogeneous scope designation of the scenarios, K-distribution, known for handling more complex data patterns, was estimated using Maximum Likelihood (ML) to determine the parameters. $(\tilde{v}_K, \tilde{\mu}_{\xi^2}) = \arg\max_{v_K, \mu_{\xi^2}} \left\{\ln\left[l_{n_{smp}}\left(v_K, \mu_{\xi^2}; \xi_1, \xi_{2,\cdots,}\xi_{n_{smp}}\right)\right]\right\}$. The log-likelihood function used was: $\ln\left[l_{n_{smp}}\left(v_K, \mu_{\xi^2}; \xi_1, \xi_{2,\cdots,}\xi_{n_{smp}}\right)\right] = v_K \sum_{q=1}^{n_{smp}} \ln \xi_q + \sum_{q=1}^{n_{smp}} \ln\left\{K_{vk-1}\left[2\,\xi_q\sqrt{\frac{v_K}{\mu_{\xi^2}}}\right]\right\} + n_{smp}\left[v_K + \frac{1}{2}\ln\left(\frac{v_K}{\mu_{\xi^2}}\right) + \ln 4 - \ln\Gamma(v_K)\right]$; in this effort, the results for the K-distribution led to: $\tilde{v}_K \approx 70.143$ and $\tilde{\mu}_{\xi^2} \approx 194.919$.

As a concluding remark, the high value of $\tilde{v}_K$ suggests that the K-distribution may not be the most appropriate model for the dataset, potentially due to numerical issues or the specific characteristics of the data. The Rayleigh distribution, on the other hand, was prone to producing erroneous reasoning.

3. Results

3.1. Case 1: Band 2 VHR SAR HH (raw - Speckle)

The comprehensive statistical analysis of Very High-Resolution (VHR) Synthetic Aperture Radar (SAR) datasets, particularly focusing on HH polarization, revealed significant differences in key metrics. These differences are accentuated in four distinct cases, which are critical for assessing the scattering model of a metallic-roof building with specific viewing directions: Band 2 VHR SAR HH, raw and Speckle (Lee *et al*., 1994), Band 2 GLCM Contrast (Speckle and iterated), Band 2 GLCM Contrast and GLCM Dissimilarity and Band 2 GLCM Dissimilarity and GLCM Entropy.

By employing the Shi-Tomasi method, centroid detection acquired a significant number of interest points in the image, exhibiting specific statistical properties, with a calculated mean position (595.0685, 589.9018), variance σ_x^2 in the *x*-direction $\approx$ 14612.22 and in the y direction (σ_y^2) $\approx$ 9111.462. The standard deviation *x*-*y* ratio $\approx$ 120.881 − 95.45398, also ranging with the highest-lowest value 4 − 1032, whilst for *y*,

1039 − 73. As shown in Figure 20, the skewness and kurtosis for the first dataset are 0.72 and 1.15, respectivily, suggesting a slight positive skew and a relatively flat distribution.

Remarkably, the speckle data shows higher skewness (0.99) and kurtosis (2.69), indicating a more pronounced positive skew and heavier tails.

The correlation coefficient of 0.658 suggests a moderate positive correlation. For each frame in a sequence, slight movements were simulated by shifting the points according to the relationship $\mu - \sigma$.

The comparative visualization of $\mu - \sigma$ metrics in HH polarization, continuously illustrated in Figure 20, shows the relationship between Band 2 amplitude and corresponding features such as skewness and kurtosis. The correlation coefficient R^2 = 0.658 further highlights the moderate positive correlation, with interpolated accelerations of tracked points contributing to the analysis.

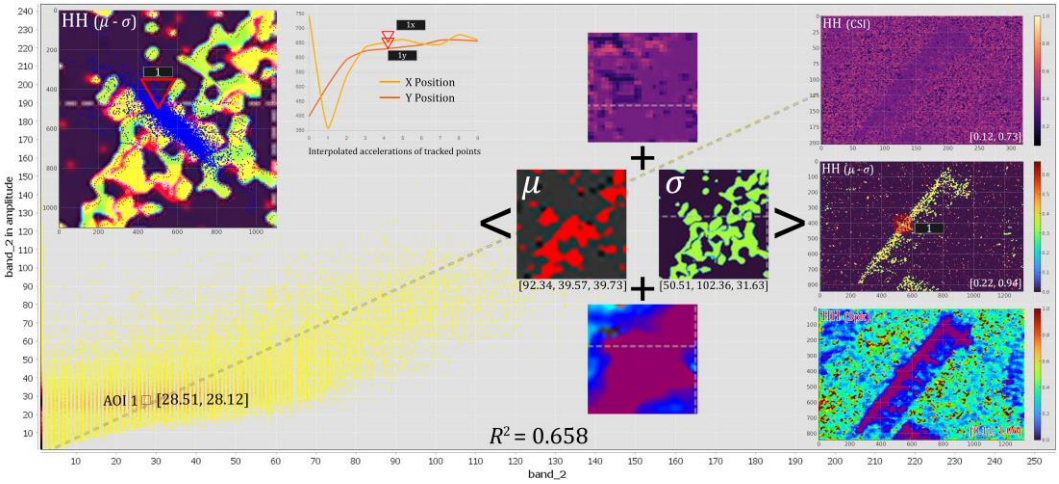

Figure 20. Correlation Analysis of SAR Data with Speckle Noise

The Kalman filter required is defined by the equations: the Kalman Gain (K_k) is given by $K_k = P_{k|k-1}H^T(HP_{k|k-1}\,H^T + R)^{-1}$, the state update ($\hat{x}_{k|k}$) is given by $\hat{x}_{k|k-1} + K_k(z_k - H\,\hat{x}_{k|k-1})$ and the covariance update ($P_{k|k}$) is given by $(I - K_k\,H\,P_{k|k-1})$.

In this pattern augmentation context, the sorted values used as indicators for Kalman execution were primarily Process Variance (Q) of 1e-5 and Measurement Variance (R) of 1e −1. These variances were chosen to balance the process noise and measurement noise (Tsuchida *et al*., 2003).

3.2. Case 2: Band 2 GLCM Entropy (Speckle – GLC)

The error distribution and effectiveness, whilst the array of variable *n* has been iteratively rescaled, denotes the total number of data points, via Mean Squared Error (MSE).

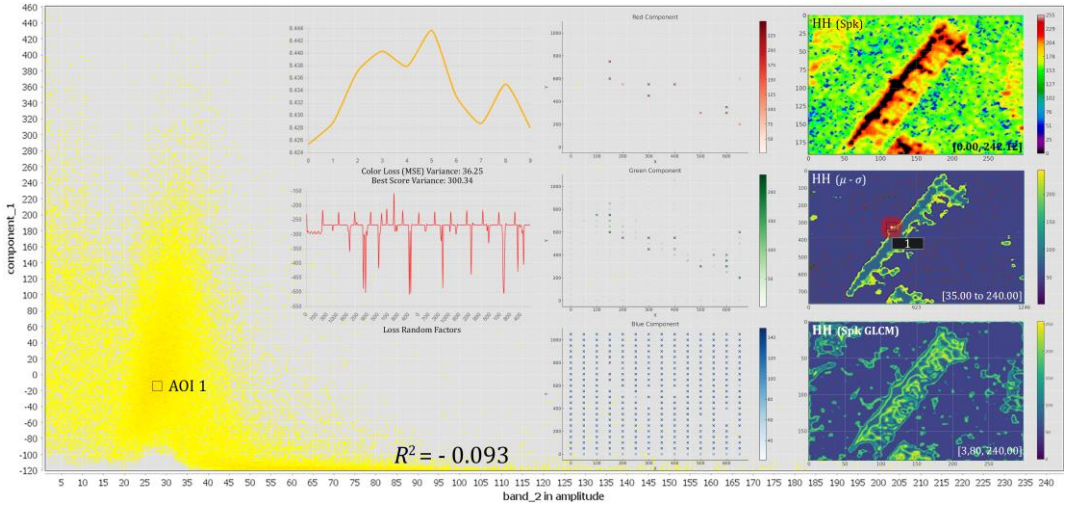

Figure 21. Analysis of GLCM and Speckle Noise in SAR Data

Whereas the discrepancies in the VHR SAR $\mu - \sigma$ actual color values are discriminated for the *i*-th data point, and also denote in correspondence of the predictions, larger values and higher dispersions, indicating error of distribution. As shown in Figure 21, the prediction accuracy reveals significant statistical deviations, despite preprocessing strategies such as color normalization and GLCM skewness and kurtosis, (2.24 and 8.75, respectively), which suggest a highly positive skew and outline the most optimal output quality.

In contrast, Speckle data shows a skewness of -0.43 and kurtosis of 4.83, indicating a slight negative skew and a distribution with heavier tails. The correlation coefficient of -0.093 suggests almost no linear relationship between the columns. Adjustment to the loss function guided modifications, such as incorporating RGB channel-specific loss terms, to refine the initial model.

3.3. Case 3: Band 2 GLCM PCA and GLCM Dissimilarity

The GLCM-PCA correlation, presented in Figure 22, reinforces the observation of a highly skewed distribution. For the second component, the variance and std. dev. 2.97 × 10^{32} and 1.72 × 10^{16}, respectively, while for the other, 9.06 × 10^{31} and 9.52 × 10^{15}.

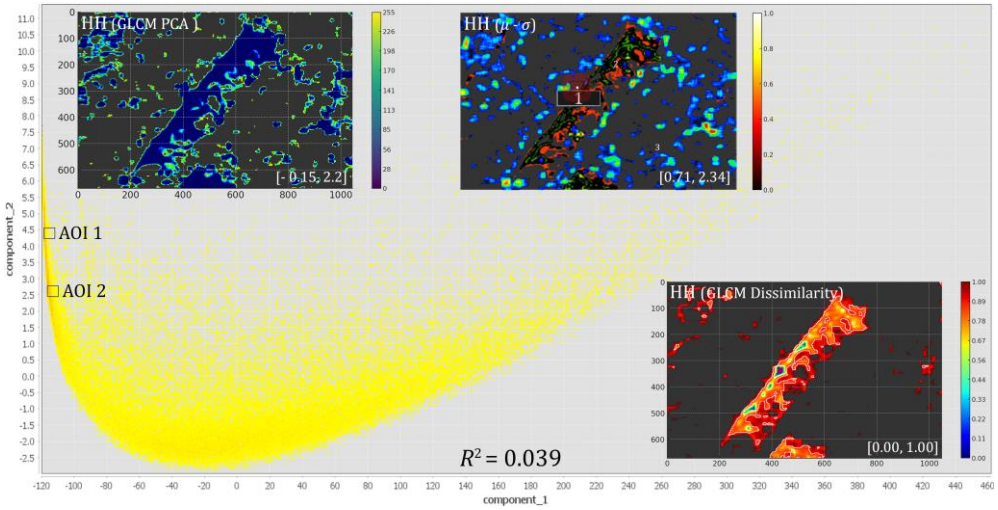

Figure 22. GLCM PCA and Dissimilarity Analysis in SAR Data

This refinement confirmed the Area of Interest (AOI), ensuring a smoothed estimate of the tracked points, while the process variance indicates the expected noise variability of the system, independent of the measurements.

As previously confirmed, a higher value for the Kalman filter was considered a flexible and responsive alternative in evaluating target signatures in radar Optical/SAR modelling within dense and sparse clusters. The analysis also synthetizes the values of skewness and kurtosis in terms of Entropy, respectively − 0.40 and 4.26, suggesting a slight negative skew and significant outliers. Regarding dissimilarity, we observe a skewness of 1.90 and kurtosis of 4.80, indicating a pronounced positive skew and heavier tails; in the last instance, the correlation coefficient of 0.039 suggests no linear association between the datasets.

Corroborating this confirmation of the statistical distribution of Entropy and dissimilarity metrics within HH polarization, we conclude that the Entropy analysis reveals a slight negative skew and significant outliers, while the dissimilarity metric exhibits a pronounced positive skew with heavier tails. The correlation coefficient, R^2 = 0.039, in fact, suggests a lack of linear association between the examined datasets, indicating the complexity of the relationships between the principal components.

3.4. Case 4: Band 2 GLCM Dissimilarity and GLCM Entropy

The fourth case, examined in Figure 23, iterates a GLCM Dissimilarity's mean is 4.31×10^{15} and Entropy's mean is 4.10×10^{14}; the median values are 3.01×10^{-1} for first and -3.89×10^{-2} for the second, showing a highly skewed distribution for the latter: Variance and standard deviation for Dissimilarity are 1.11×10^{32} and 1.05×10^{16}, respectively, whilst for the second, they are 8.37×10^{30} and 2.89×10^{15}.

Visually, the cluster points exhibit compactness with a slight diagonal scatter; nevertheless, the *R*-squared value indicates that the model's predictive utility is limited.

Hence, as confirmed in the Figure 23, the skewness and kurtosis are 1.87 and 4.11, respectively, suggesting a pronounced positive skew and significant outliers; for Entropy, a skewness of 3.69 and kurtosis of 25.31, contributing to a positive skew and very heavy tails.

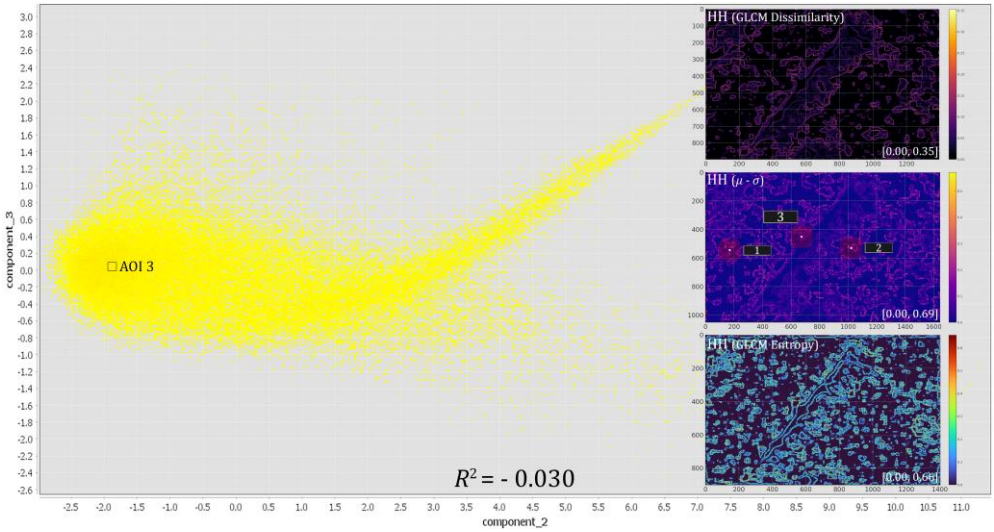

Figure 23. Analysis of GLCM Dissimilarity and Entropy in SAR Data

The correlation coefficient of − 0.030 suggests almost no linear relationship between the Dissimilarity and Entropy while the statistical exploration of component 2 is focused on GLCM metrics. In this instance, the dissimilarity metric shows a pronounced positive skew with significant outliers, while the Entropy metric displays an even stronger positive skew with very heavy tails.

To amalgamate these results, we notice that the correlation coefficient, $R^2 = -0.030$, indicates an almost negligible linear relationship between the Dissimilarity and Entropy, highlighting the complex nature of their interaction within the SAR dataset.

3.5. Impact of feature selection on Error Prediction in VHR SAR data

The analysis of input-driven clusters reveals significant variance among clusters in predicting errors, with Cluster 0 consistently showing the highest impact across all images. As visually outlined in Figure 24 we observe that this consistent performance of Cluster 0 emphasizes its critical role as the Optical ground truth. Conversely, the minimal impact displayed by the other clusters raises questions about their relevance in the predictive model, concerning Band 2 VHR SAR HH - Speckle data: the sharp decline in feature impact from Cluster 0 to other clusters suggests a potential over-reliance on a single cluster.

In support of this over-reliance, we may be orientated to consider a suboptimal model performance, especially when considering the impacts of feature selection methods on urban impervious surface extraction using optical and SAR data; to connect these results to the urban surface extraction, we incorporated the most balanced and comprehensive multistage framework in predictive modelling as explored by Weng (2016).

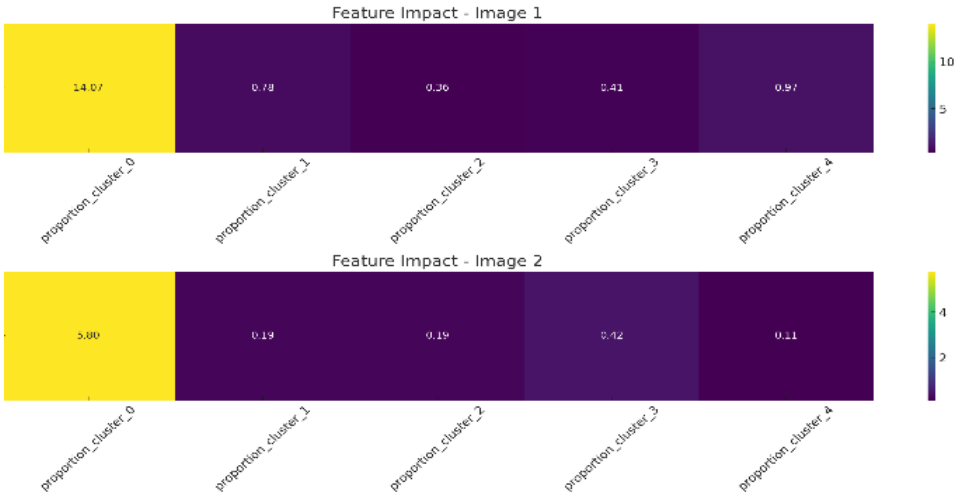

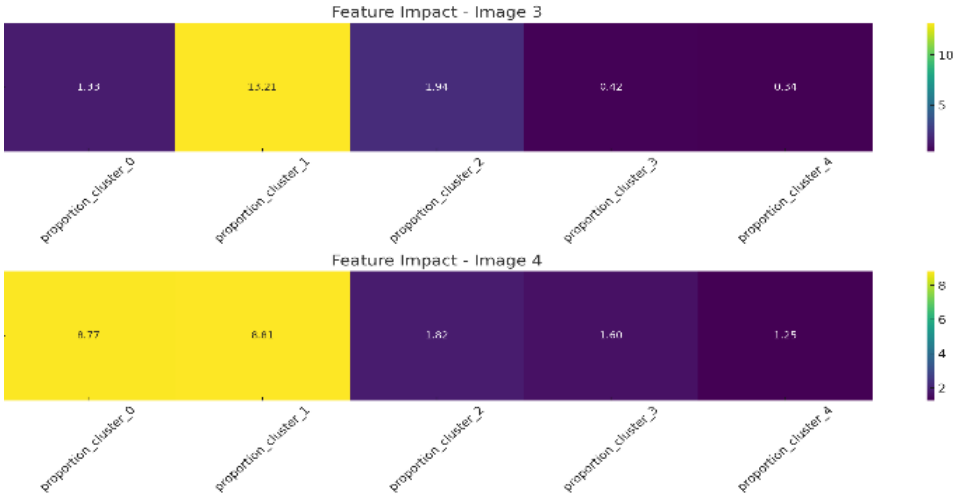

Figure 24. Multistage Feature Impact Analysis Across Clusters

3.6. Prediction Error in Segmented VHR Images with Intensity Histograms

To reinforce the Multistage impact throughout the refinements, we gather a second overall mosaic, having as an object the combined analysis of pixel intensity distributions over-prediction errors.

The comparison between original and segmented images reveals how segmentation affects image properties and the prediction error histograms further elucidate the impact on model performance.

Specifically, these histograms compare the pixel intensity distributions between the original images and the segmented images across four different cases:

i) for Figure 25 (a), VHR SAR HH (raw - Speckle), the *x*-axis represents pixel intensity values, while the *y*-axis indicates their frequency, with the blue and red colours corresponding to the original and segmented images, respectively. The segmentation introduces significant shifts in intensity distribution, suggesting alterations in the image's structure or features, which are crucial for downstream tasks like object detection or classification. The corresponding Prediction Error histogram in Figure 25 (b) shows that segmentation leads to more pronounced red peaks in certain intensity ranges, indicating a concentration of pixel values.

This suggests that segmentation may amplify certain features or smooth out variability, resulting in a more clustered intensity distribution; in last instance, the overall impact of segmentation is evident in the altered frequency of intensity values, where certain areas of the image are emphasized or blended differently than in the original image.

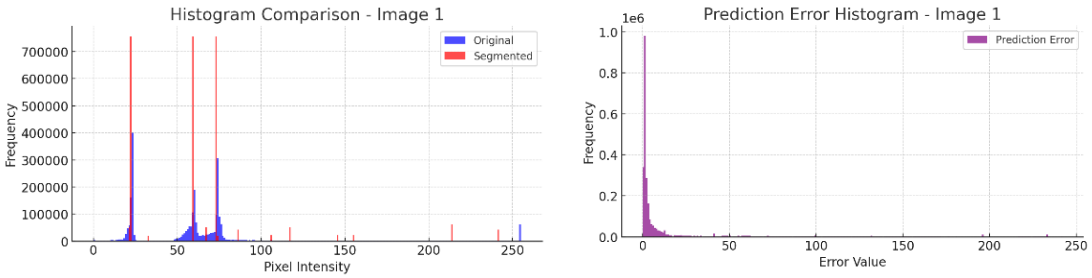

Figure 25 (a) VHR SAR HH (raw – Speckle) **(b)** Prediction Error

ii) the second pair GLCM Entropy (Speckle – GLC), presented in Figure 26 (a), indicates that the overlap between the original and segmented histograms suggests that the segmentation process has preserved some of the original intensity characteristics, particularly around certain intensity values.

Nonetheless, the differences in height and spread indicate that the segmentation has altered the distribution to some extent, potentially due to the impact of the GLCM Entropy with Speckle noise.

On the other hand, the segmented image shows slightly broader peaks, indicating that the segmentation process may have introduced some smoothing or blending of pixel values, leading to less distinct intensity groupings compared to the original image. This could be a result of the speckle noise reduction or the segmentation algorithm itself.

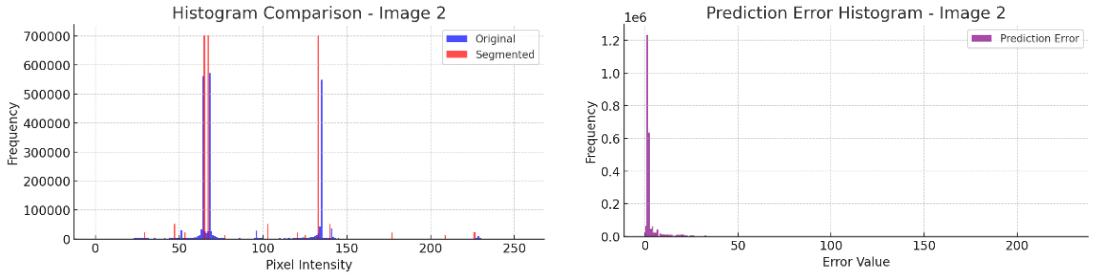

Figure 26 (a) GLCM Entropy (Speckle – GLC) **(b)** Prediction Error

iii) related to GLCM PCA and GLCM Dissimilarity in Figure 27 (a), the histogram shows a significant difference in intensity distribution after segmentation, particularly in the lower intensity range, where the red peaks indicate a higher frequency of certain pixel values in the segmented image.

This confirms that the segmentation process may have concentrated pixel values around specific intensities, altering the image's structure, which is critical for tasks like object detection or classification.

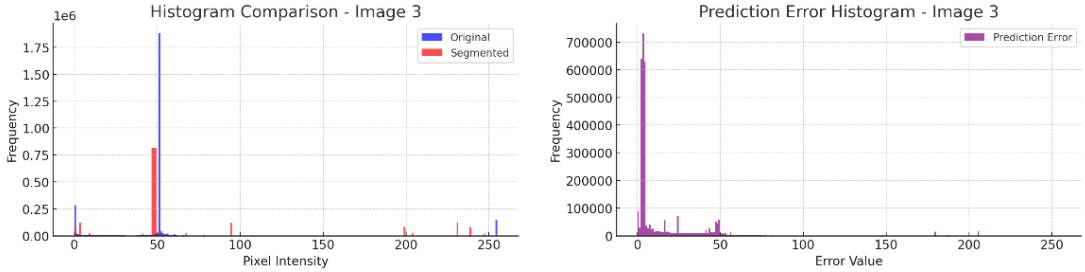

Figure 27 (a) GLCM Entropy (Speckle – GLC). **(b)** Prediction Error

iv) in the fourth case, visualized in Figure 28 (a), GLCM Dissimilarity and GLCM Entropy, there are distinct differences between the two distributions, with the segmented image showing noticeable shifts in the frequency of certain intensity ranges. The segmentation process has altered the distribution of pixel intensities, particularly in the lower intensity ranges (around 40-60), where the segmented image shows higher frequencies compared to the original.

This suggests that segmentation has concentrated pixel values around certain intensities, potentially smoothing or emphasizing particular features while most of the

prediction errors (b) are clustered near zero, concluding that the segmentation has preserved much of the original image's predictive accuracy.

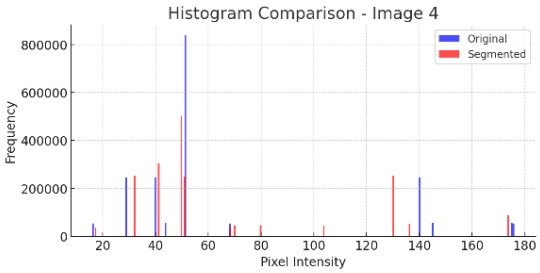

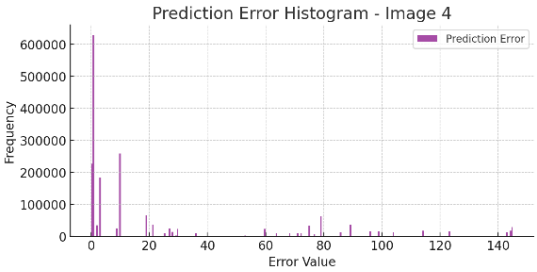

Figure 28 (a) GLCM (Dissimilarity – Entropy) **(b)** Prediction Error

4. Discussion

The study presents professional opportunities for future investigation, comparing various possibilities for advancing VHR SAR applications. Developing low-cost, user-friendly tools and expanding to diverse heritage sites can enhance accessibility and generalizability. Integrating machine learning, AI and real-time processing will automate and improve analysis. Long-term monitoring and multilateral agreements for data standardization can optimize global heritage protection. Interministerial collaborations and centralized SAR data repositories can facilitate resource sharing and enhance research impact. Exploring different radar frequencies and adaptive imaging techniques will broaden SAR capabilities. In the last instance, public-private partnerships, community engagement and policy-driven research can ensure sustainable heritage conservation and technological advancements.

5. Conclusion

Design is critical to advancing the capabilities in Very High-Resolution Synthetic Aperture Radar technology for impervious surface extraction. The design-centric approach of the study shows the way in which advanced statistical methods comprise Rayleigh, Nakagami and K-distributions integrated with Gray Level Co-occurrence Matrix, Principal Component Analysis and Gabor filters that are able to enhance radar image processing. These design methodologies create the ability to optimize SAR data in complex urban environments, building both detection accuracy and situational awareness.

The application of design principles within the SAR technology offers innovative solutions to the challenges brought about by rapidly changing, hostile environments.

This research effectively uses GLCM, PCA and Kalman filtering to refine the textural analysis and reduce noise for such scenarios where the demands cannot usually be met with traditional methods by employing a design-driven strategy. The design methodology enhances target tracking and material characterization, hence improving robustness and reliability in radar systems for urban monitoring and defense applications.

Furthermore, the research is envisaging the use of design-oriented approaches that will encapsulate a number of environmental and material factors. In this work, Nakagami-K-distribution models assist in the improvement of knowledge concerning the spatial distribution and variability of radar images in an urban multipath scenario. The focus on design here permits more correct interpretation of radar signals, enables better feature extraction and allows for the creation of new standards in environmental monitoring as

well as electronic warfare. These findings are poised to underscore how a design-driven approach in the application of VHR SAR technology is set to transform its development.

With such advanced design methods, the gap is bridged between theoretical modelling and practical application, showing that in fact, design is a valid factor which can add significantly first to the effectiveness and secondly to the operational performance of the radar systems in overcoming the limitations presented by complicated urban and natural environments. This is an approach that not only advances technology in radar but also lends great enhancement to the application of wider fields in environmental management and defence.

References

Akaike, H. (1974). A new look at the statistical model identification. *IEEE Transactions on Automatic Control, 19*(6), 716–723. https://doi.org/10.1109/TAC.1974.1100705

Abdulla, K., & Abdelmonem, M. G. (2023). Mapping Safety, Security and Walkability of Historical Public Open Spaces in Post-Conflict Libya: Tripoli as North African Case Study. *Journal of Contemporary Urban Affairs*, *7*(2), 85–105. https://doi.org/10.25034/ijcua.2023.v7n2-6

Bouziani, M., Goïta, K. & He, D.C. (2010). Automatic change detection of buildings in urban environment from very high spatial resolution images using existing geodatabase and prior knowledge. *ISPRS Journal of Photogrammetry and Remote Sensing*, *65*(1), 143–153. https://doi.org/10.1016/j.isprsjprs.2009.10.002

Chang, L., Wang, L., Wang, W., Liu, G. & Ling, X. (2016). Akaike information criterion-based objective for belief rule base optimization. In *2016 8th International Conference on Intelligent Human-Machine Systems and Cybernetics (IHMSC)*, 545–549. Hangzhou, China. https://doi.org/10.1109/IHMSC.2016.83

Chen, X., Dong, Z., Zhang, Z., Tu, C., Yi, T. & He, Z. (2024). Very high resolution synthetic aperture radar systems and imaging: A review. *IEEE Journal of Selected Topics in Applied Earth Observations and Remote Sensing*, 17, 7104–7123. https://doi.org/10.1109/JSTARS.2024.3374429

Christaki, M., Vasilakos, C., Papadopoulou, E.E., Tataris, G., Siarkos, I. & Soulakellis, N. (2022). Building change detection based on a gray-level co-occurrence matrix and artificial neural networks. *Drones*, *6*(12), 414. https://doi.org/10.3390/drones6120414

Dabiri, Z., Hölbling, D., Lang, S. & Bartsch, A. (2015). Applicability of multi-seasonal X-band SAR imagery for multiresolution segmentation: A case study in a riparian mixed forest. *The International Archives of the Photogrammetry, Remote Sensing and Spatial Information Sciences, XL-1/W5*, 123–128. https://doi.org/10.5194/isprsarchives-XL-1-W5-123-2015

Dong, L., Shan, J. (2013). A comprehensive review of earthquake-induced building damage detection with remote sensing techniques. *ISPRS Journal of Photogrammetry and Remote Sensing*, 84, 85–99. https://doi.org/10.1016/j.isprsjprs.2013.06.011

Esch, T., Schenk, A., Thiel, M., Ullmann, T., Schmidt, M. & Dech, S. (2010). Land cover classification based on single-polarized VHR SAR images using texture information derived via speckle analysis. In *2010 IEEE International Geoscience and Remote Sensing Symposium*, 1875–1878. Honolulu, HI, USA. https://doi.org/10.1109/IGARSS.2010.5650031

Ferro, A., Brunner, D. & Bruzzone, L. (2013). Automatic detection and reconstruction of building radar footprints from single VHR SAR images. *IEEE Transactions on Geoscience and Remote Sensing, 51*(2), 935–952. https://doi.org/10.1109/TGRS.2012.2205156

Fotohabady, V., Said, F. (2011). Comparison of the Rayleigh and Nakagami fading channels MIMO multicarrier system. In *2011 Wireless Advanced*, 295–300. London, United Kingdom. https://doi.org/10.1109/WiAd.2011.5983272

Gabor, D. (1946). Theory of communication. *Journal of the Institution of Electrical Engineers - Part III: Radio and Communication Engineering, 93*(26), 429–457.

Gokon, H., Koshimura, S. & Meguro, K. (2017). Towards a damage assessment in a tsunami affected area using L-band and X-band SAR data. In *2017 Joint Urban Remote Sensing Event (JURSE)*, 1–4. Dubai, United Arab Emirates. https://doi.org/10.1109/JURSE.2017.7924633

Gomes, N.R., Dammert, P., Pettersson, M.I., Vu, V.T. & Hellsten, H. (2019). Comparison of the Rayleigh and K-distributions for application in incoherent change detection. *IEEE Geoscience and Remote Sensing Letters, 16*(5), 756–760. https://doi.org/10.1109/LGRS.2018.2881733

Goriachkin, O.V., Borisenkov, A.V., Gusev, N.A. & Lifanov, A.S. (2022). SAR system for searching and detecting objects in the forest area, based on UAVs. In *2022 VIII International Conference on Information Technology and Nanotechnology (ITNT)*, 1–4. Samara, Russian Federation. https://doi.org/10.1109/ITNT55410.2022.9848634

Greenspan, R. (1971). Testing a sample population for the Rayleigh distribution. *IEEE Transactions on Communications, 19*(1), 99–100. https://doi.org/10.1109/TCOM.1971.1090606

Hussain, M., Chen, D., Cheng, A., Wei, H. & Stanley, D. (2013). Change detection from remotely sensed images: From pixel-based to object-based approaches. *ISPRS Journal of Photogrammetry and Remote Sensing*, 80, 91–106. https://doi.org/10.1016/j.isprsjprs.2013.03.006

Janalipour, M., Taleai, M. (2017). Building change detection after earthquake using multi-criteria decision analysis based on extracted information from high spatial resolution satellite images. *International Journal of Remote Sensing, 38*(1), 82–99. https://doi.org/10.1080/01431161.2016.1259673

Kuruoglu, E.E., Zerubia, J. (2004). Modeling SAR images with a generalization of the Rayleigh distribution. *IEEE Transactions on Image Processing, 13*(4), 527–533. https://doi.org/10.1109/TIP.2003.818017

Lee, J.S., Jurkevich, L., Dewaele, P., Wambacq, P. & Oosterlinck, A. (1994). Speckle filtering of synthetic aperture radar images: A review. *Remote Sensing Reviews, 8*(4), 313–340. https://doi.org/10.1080/02757259409532206

Liebenberg, S., Allison, J. (2023). A review of goodness-of-fit tests for the Rayleigh distribution. *Austrian Journal of Statistics, 52*(1), 1–22. https://doi.org/10.17713/ajs.v52i1.1322

Luo, X., Bao, R., Liu, Z., Zhu, S. & Liu, Q. (2023). Super-resolution of SAR images with speckle noise based on combination of cubature Kalman filter and low-rank approximation. *IEEE Transactions on Geoscience and Remote Sensing*, 61, 1–14. https://doi.org/10.1109/TGRS.2023.3305025

Makmur, N.M., Kwan, F., Rana, A.D. & Kurniadi, F.I. (2023). Comparing local binary pattern and gray level co-occurrence matrix for feature extraction in diabetic retinopathy classification. *Procedia Computer Science*, 227, 355–363. https://doi.org/10.1016/j.procs.2023.10.534

Martín-de-Nicolás, J., Jarabo-Amores, M.P., Mata-Moya, D., Del-Rey-Maestre, N. & Bárcena-Humanes, J.L. (2014). Statistical analysis of SAR sea clutter for classification purposes. *Remote Sensing, 6*(10), 9379–9411. https://doi.org/10.3390/rs6109379

Mesleh, R., Badarneh, O. & Younis, A. (2022). Nakagami-m MIMO channel model. In *2022 9th International Conference on Electrical and Electronics Engineering (ICEEE)*, 280–284. Alanya, Turkey. https://doi.org/10.1109/ICEEE55327.2022.9772568

Ning, X., Zhang, H., Zhang, R. & Huang, X. (2024). Multi-stage progressive change detection on high-resolution remote sensing imagery. *ISPRS Journal of Photogrammetry and Remote Sensing*, 207, 231–244. https://doi.org/10.1016/j.isprsjprs.2023.11.023

Odunlade, O., & Abegunde, A. A. (2023). Territoriality in Post-conflict Neighbourhoods: Unravelling the Dynamics of Territorial Marks in Ile-Ife, Nigeria. *Journal of Contemporary Urban Affairs*, *7*(1), 69–85. https://doi.org/10.25034/ijcua.2023.v7n1-5

Peng, L.B., Wang, Y.Q., Chen, Y.P. & Peng, Z.M. (2023). SAR target detection based on the optimal fractional Gabor spectrum feature. *Journal of Electronic Science and Technology*, *21*(2), 100197. https://doi.org/10.1016/j.jnlest.2023.100197

Pluto-Kossakowska, J., Grandgirard, D. & Kerdiles, H. (2007). Assessment of parcel area measurement based on VHR SAR images. In *RSPSoc 2007: Conference of the Remote Sensing and Photogrammetry Society*, 1, 426. Curran Associates, Inc..

Puetz, A.M., Olsen, R.C. (2006). Haralick texture features expanded into the spectral domain. In *Proceedings of the Society of Photo-Optical Instrumentation Engineers (SPIE)*, 623311. Orlando (Kissimmee), FL. https://doi.org/10.1117/12.665699

Reba, M., Seto, K.C. (2020). A systematic review and assessment of algorithms to detect, characterize, and monitor urban land change. *Remote Sensing of Environment*, 242, 111739. https://doi.org/10.1016/j.rse.2020.111739

Ruiz, E.F., Chaparro-Arce, D., Pantoja, J.J., Vega, F., Kasmi, C. & Al Yafei, F. (2020). Ground penetrating radar radargram filter using singularity expansion method. In *2020 International Applied Computational Electromagnetics Society Symposium (ACES)*, 1–2. Monterey, CA, USA. https://doi.org/10.23919/ACES49320.2020.9196132

Sagrillo, M., Guerra, R.R., Bayer, F.M. & Machado, R. (2022). A new probability distribution for SAR image modeling. *Remote Sensing*, *14*(12), 2853. https://doi.org/10.3390/rs14122853

Salo, J., El-Sallabi, H.M. & Vainikainen, P. (2006). The distribution of the product of independent Rayleigh random variables. *IEEE Transactions on Antennas and Propagation*, *54*(2), 639–643. https://doi.org/10.1109/TAP.2005.863087

Shahzad, M., Maurer, M., Fraundorfer, F., Wang, Y. & Zhu, X.X. (2019). Buildings detection in VHR SAR images using fully convolutional neural networks. *IEEE Transactions on Geoscience and Remote Sensing*, *57*(2), 1100–1116. https://doi.org/10.1109/TGRS.2018.2864716

Singh, M., Kaur, G. (2011). SAR image classification using PCA and texture analysis. In *Information Technology and Mobile Communication*, 147, 435–439. Berlin, Heidelberg: Springer Berlin Heidelberg. https://doi.org/10.1007/978-3-642-20573-6_78

Soh, L.K., Tsatsoulis, C. (1999). Texture analysis of SAR sea ice imagery using gray level co-occurrence matrices. *IEEE Transactions on Geoscience and Remote Sensing*, *37*(2), 780–795. https://doi.org/10.1109/36.752194

Subrahmanyam, G.R.K.S., Rajagopalan, A.N., Aravind, R. & Rigoll, G. (2008). Edge-preserving unscented Kalman filter for speckle reduction. In *2008 19th International Conference on Pattern Recognition*, 1–4. Tampa, FL, USA. https://doi.org/10.1109/ICPR.2008.4761408

Softaoğlu, H. (2019). Scrutinising The Production Of Space On The Example Of Regent Street and Painting A Modern Life By The Agencies Of Regency. *Journal of Contemporary Urban Affairs*, *3*(3), 51–66. https://doi.org/10.25034/ijcua.2019.v3n3-5

Tegos, S.A., Tyrovolas, D., Diamantoulakis, P.D., Liaskos, C.K. & Karagiannidis, G.K. (2022). On the distribution of the sum of double-Nakagami-m random vectors and application in randomly reconfigurable surfaces. *IEEE Transactions on Vehicular Technology*, *71*(7), 7297–7307. https://doi.org/10.1109/TVT.2022.3164846

Tsuchida, M., Haseyama, M. & Kitajima, H. (2003). A Kalman filter using texture for noise reduction in SAR images. *Electronics and Communications in Japan (Part I: Communications)*, *86*(10), 21–32. https://doi.org/10.1002/ecja.10065

Wang, Z., Bovik, A.C. (2009). Mean squared error: Love it or leave it? A new look at signal fidelity measures. *IEEE Signal Processing Magazine*, *26*(1), 98–117. https://doi.org/10.1109/MSP.2008.930649

Yang, F., Yang, X., Wang, Z., Lu, C., Li, Z. & Liu, Y. (2019). Object-based classification of cloudy coastal areas using medium-resolution optical and SAR images for vulnerability assessment of marine disaster. *Journal of Oceanology and Limnology*, *37*(6), 1955–1970. https://doi.org/10.1007/s00343-019-8266-y

Zhang, X., Xiao, K. & Gu, J. (2022). *Theory to Countermeasures against New Radars*. Singapore: Springer Nature Singapore. https://doi.org/10.1007/978-981-16-6715-2